Effects of Satellite Revisit Rate and Time-Series Smoothing Method on Throughout-Season Maize Yield Correlation Accuracy

Emily Myers, *Graduate Student Member, IEEE*, John Kerekes, *Senior Member, IEEE*, Craig Daughtry, and Andrew Russ

***Abstract*—Predictions of crop yield made during the growing season aid in crop management and economic planning. Many yield prediction models are made by performing regression between satellite-derived vegetation indices (VI) and yield. This article studied the effects of time-series end date and satellite imaging frequency on the accuracy of VI-yield correlation. Daily, 3-m resolution, multispectral images were obtained over a maize field near Beltsville, MD, USA, in 2018 and 2019. Plot-average green normalized difference vegetation index (GNDVI) was extracted from these images. GNDVI time-series data were resampled to different revisit intervals, gap-filled and smoothed, temporally realigned, and correlated with plot-average yield at every day of the growing season. These experiments were then repeated with data removed from the end of the time-series. All methods tested performed well on time-series ending 72 d or more after green-up in 2019 (R-squared = 0.95) or time-series ending 65 d or more after green-up in 2018 (Flexfit R-squared = 0.92; shape model fitting R-squared = 0.89). All methods had poor correlation for time-series ending prior to the day of peak GNDVI. Mean R-squared values for GNDVI-yield correlations decreased with increasing revisit intervals. These trends were stronger in the 2019 data, with mean R-squared decreasing by more than 0.05 when sampled from 1 to 30-d revisit intervals (Flexfit) or to 22-d revisit intervals (shape model fitting). These findings, along with cloud-contamination statistics, were used to recommend an optimal methodology for yield correlation and an optimal overpass frequency of 1–4 d for future yield-monitoring satellite systems.**

***Index Terms*—Agriculture, CubeSats, maize, multispectral, PlanetScope, remote sensing, yield estimation.**

I. Introduction

ACCURATE and early prediction of crop yield can help farmers more effectively manage their fields—by addressing water stress, nutrient deficiencies, and other issues that may affect yields at harvest—as well as aid in economic planning. While crop measurements used in yield prediction models may be collected manually, remote sensing-based yield prediction models have gained popularity due to their potential to be lower cost and ability to cover large areas of land more quickly and frequently than ground-based methods. These models often work by collecting multi- or hyperspectral imagery over a field during the growing season, deriving a quantity—often a vegetation index (VI)—from the imagery, and putting that quantity into an equation—often a linear [1]–[4] or exponential [3] function, although sometimes more complicated equations are used [5]–[8]—that relates it to the yield of the relevant pixel, plot, or field.

Many yield prediction models rely on satellites that deliver frequent imagery because they are better equipped to capture rapid changes in vegetation growth and health. Commonly used satellites for yield prediction include the National Oceanic and Atmospheric Administration (NOAA) advanced very high resolution radiometer (AVHRR) and the National Aeronautics and Space Administration moderate resolution imaging spectroradiometer (MODIS). Both offer daily global coverage at moderate spatial resolutions (AVHRR: 1.1 km, MODIS: 250–1000 m). Multiple researchers have found correlations between MODIS-derived indices and crop yield, with relevant studies that include: Correlating maize and soybean yield with measurements of two-band enhanced vegetation index (EVI2), normalized difference water index, and normalized difference vegetation index (NDVI) a number of days after vegetation green-up [1]; correlating maize yield with green leaf area index (LAIg) derived from the wide dynamic range vegetation index (WDRVI) measured during the mid-grain filling stage [2]; correlating maize yield with NDVI calculated at its peak value in the growing season [3]; and correlating maize yield with WDRVI measured 7 d before the start of the silking stage [4]. Using AVHRR images, researchers have related maize yield with vegetation condition index (VCI) and temperature condition index (TCI) measured six weeks before harvest [9]. Finer-resolution satellites like Landsat 7 and Landsat 8, which have 30-m bands in the visible and near-infrared (VNIR) wavelengths, or Sentinel-2 A and Sentinel-2B, which have 10–20-m bands in the VNIR wavelengths, have also been used for yield prediction [7], [10]. Although these satellites are better suited to imaging small or heterogeneous plots, their longer revisit rates (Landsat 7 and 8: 16 d each or 8 d combined, Sentinel-2: 10 d each or 5 d combined) mean that they do not

Manuscript received July 23, 2021; revised September 17, 2021, September 29, 2021, and October 23, 2021; accepted November 8, 2021. Date of publication November 18, 2021; date of current version December 6, 2021. This work was supported in part by the National Aeronautics and Space Administration under Grant NNX14AP40G and in part by the U.S. Department of Agriculture, Agricultural Research Service. USDA is an equal opportunity provider and employer. *(Corresponding author: Emily Myers.)*

Emily Myers and John Kerekes are with the Chester F. Carlson Center for Imaging Science, Rochester Institute of Technology, Rochester NY 14623 USA (e-mail: em2521@rit.edu; kerekes@cis.rit.edu).

Craig Daughtry and Andrew Russ are with the USDA-ARS Hydrology and Remote Sensing Laboratory, Beltsville MD 20705 USA (e-mail: craig.daughtry@usda.gov; andrew.russ@usda.gov).

Digital Object Identifier 10.1109/JSTARS.2021.3129148

always collect images frequently enough to capture information at crucial growth stages.

There are several ways to obtain imagery that is high in both spatial and temporal resolution. One way is by combining data from multiple sensors. Such efforts have included the fusion of Landsat 8 and MODIS data products for vegetation phenology monitoring [11]–[13] and the creation of a harmonized Landsat 8 and Sentinel-2 (HLS) data product [14], [15]. Recent advances in technology have also allowed for the development of satellite systems that collect multispectral, high spatial resolution imagery at more frequent intervals. The commercially operated PlanetScope constellation is a large collection of small, inexpensive satellites called Cubesats that capture daily imagery in blue, green, red, and near-infrared (NIR) spectral bands at approximately 3-m resolution. The French–Israeli government-operated VENμS satellite collects 12-band imagery over 123 scientific sites every other day, at 5-m resolution [16]. Cubesat imagery has been used for vegetation monitoring [17]–[21] and yield prediction [6], [22]–[24], although some researchers opt for fusion with data from other satellites like Sentinel-2 [17] or Landsat 8 and MODIS [25] to improve the radiometric quality. VEN μS has also been used, on its own and in combination with other satellites, for vegetation monitoring tasks [26], [27].

Although researchers have begun to explore the use of high-resolution ($<$10 m), high-frequency multispectral imagery for agricultural monitoring and yield prediction, the capabilities and limitations of these relatively new technologies have not yet been fully investigated. In addition to contributing to the growing body of yield prediction research using data derived from these newer satellite systems, this article aims specifically to quantify the effects of image availability on maize yield prediction accuracy. By starting with daily, high-spatial resolution imagery of a maize (*Zea mays* L.) field in the mid-Atlantic over the entire growing season and removing images from the dataset to create time-series at different revisit intervals or time-series that end partway through the growing season, it aims to answer two questions: 1) What is the relation between satellite revisit interval and mid-season maize yield correlation accuracy? 2) How does time-series end date affect maize yield correlation accuracy, i.e., how early in the growing season can image data be correlated with future yield?

The unique contributions of this research are twofold. First, where most previous yield correlation and prediction studies have used satellite imagery that is high spatial resolution and low radiometric quality (PlanetScope constellation [6], [22]–[24]), high radiometric quality and somewhat high spatial resolution (Landsat 8 and Sentinel-2 [7], [24]), or high temporal resolution and moderate spatial resolution (MODIS [2], [4]), this study uses a new image data source that is high in spatial resolution (3 m) temporal resolution (1-d revisit), and radiometric quality (consistent with Landsat 8 and Sentinel-2). Second, because daily image data are available for this study, it is possible to establish a quantitative relationship between revisit interval and yield correlation accuracy. Because the dataset for this article is small, consisting of imagery of one crop (maize) over a single study site, the article will focus on the trends in yield prediction accuracy rather than on the specific parameters of the equations used to relate VI to yield.

II. Methodology

A. Study Site

In both 2018 and 2019, maize (*Zea mays* L.) was no-till planted in rows spaced 0.76-m apart in a field with crop residues on the soil surface at the United States Department of Agriculture (USDA) Agricultural Research Service (ARS) Henry A. Wallace Beltsville Agricultural Research Center near Beltsville, MD, USA (39.02552°N, 76.82816°W). Plot layouts for both years are shown in Fig. 1. Planting occurred on 9 May in 2018 and 21 May in 2019. Best management practices for corn included applying 28 kg N/ha at planting and then additional *N* several weeks after planting, on 7 June in 2018 and on 19 June in 2019. The additional *N* rates were 0%, 25%, 50%, 100%, and 200% of the recommended rate (140 kg N/ha) in 2018, and 25%, 50%, 75%, and 100% of the recommended rate in 2019. Some of the plots were irrigated roughly two months after planting. The 2018 plots used in this experiment were 18.2 $\times$ 21 m, and the 2019 plots were 18.2 $\times$ 18 m. The 2018 crop was harvested on 26 October and the 2019 crop was harvested on 4 October.

B. Image Data Collection and Processing

Planet provided PlanetScope Level 3 Harmonized (L3H) imagery for use in this study. This data product consists of daily, cloud-masked, gap-filled surface reflectance imagery of the study site in four spectral bands (blue, green, red, and NIR) at 3-m spatial resolution. This imagery was produced in-house at Planet, using the Cubesat-enabled spatio-temporal enhancement method (CESTEM) to produce surface reflectance imagery at the radiometric quality of the HLS data product and the spatial and temporal resolution of the PlanetScope satellites [25].

Pixel-based regions of interest (ROIs) for each plot were selected and converted into mask images using ENVI 5.2 (L3Harris Geospatial, Broomfield, CO, USA). They were then loaded into MATLAB R2018b (Mathworks, Natick, MA, USA), where code extracted the day of year (DOY), plot-average VI, and standard deviation of plot-average VI for each plot in every image.

C. Yield Data Collection and Processing

For both years, a grain combine was used to harvest the full field of maize. A grain yield monitor on the combine collected and recorded information at regular time intervals about the maize yield collected during that time interval. Each instance of this information is referred to as a yield data point. Each yield data point included the ending GPS coordinates, wet mass, and moisture content of the maize harvested between that point and the previous one. Unreliable yield data points were removed prior to analysis, using the following filtering procedure.

1) Exclude points within 7 m of the field boundary.
2) Exclude points that exceed the maximum yield for maize (dry yield mass$>$17.26 metric tonnes/ha or 275 bu/acre).
3) Exclude points that are not the most common swath width (6 rows or 4.6 m, for these data) or yield offset (0 m, for these data).
4) For each point remaining after steps 1–3, calculate a local mean and standard deviation of the yield based on a

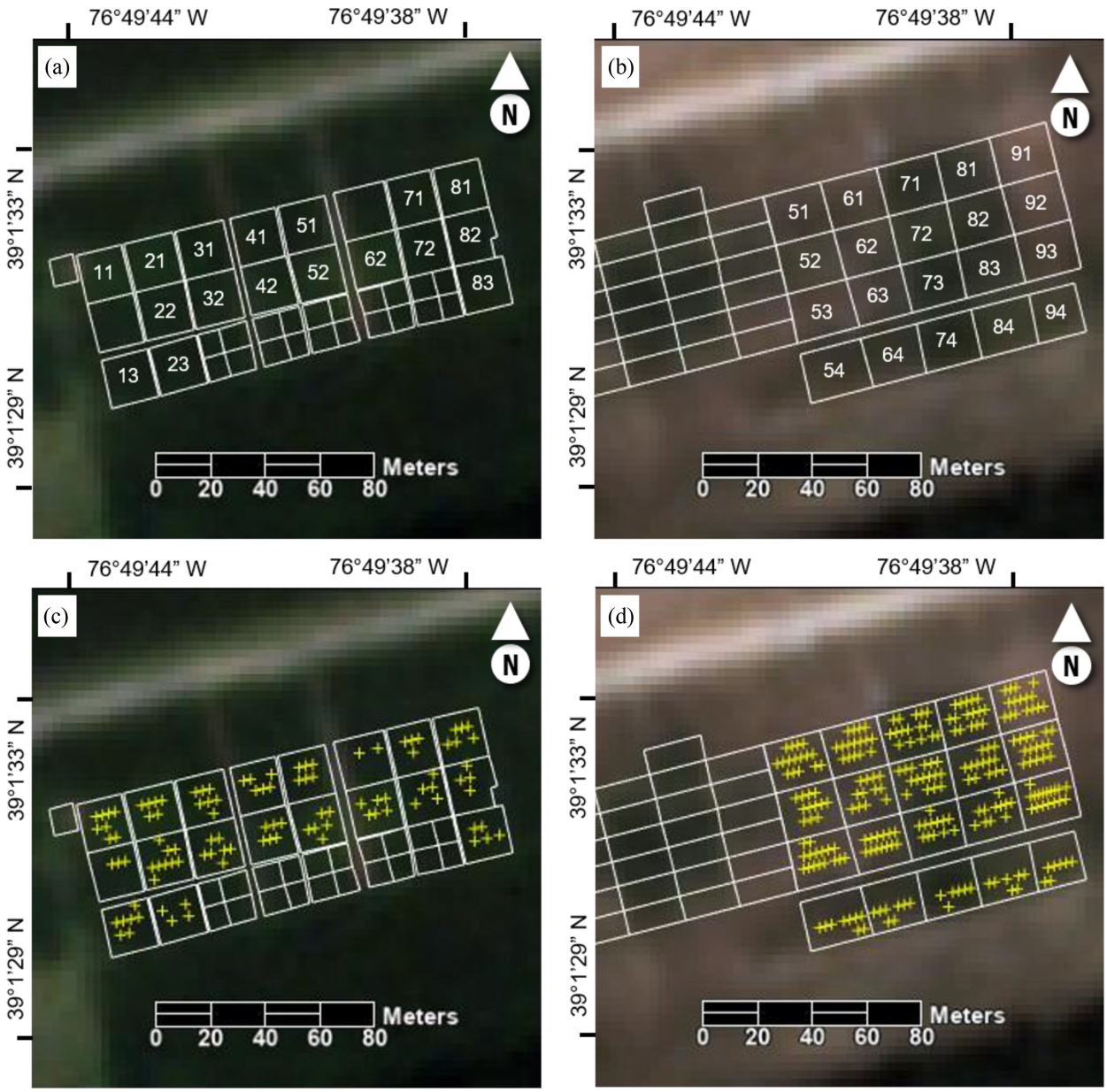

Fig. 1. View of the field and plot locations for both years. All images show RGB surface reflectance at 3-m spatial resolution, and are derived from the daily PlanetScope L3H image data product. 2019 plots are shown over an image of the field on 20 July 2019, and 2018 plots are shown over an image of the field on 20 July 2018. (a) 2019 plot layout, with numbers shown for all plots used in this study. Numbered plots are approximately 18.2 × 18 m. (b) 2018 plot layout, with numbers shown for all plots used in this study. Numbered plots are approximately 18.2 × 21 m. (c) 2019 plots with locations of yield sampling points shown in yellow. Only points that are within plot boundaries and were not removed by the filtering procedure are shown. Plots 11, 21, and 52 had the lowest average yields (2810, 4089, and 3823 kg/ha, respectively), and plots 23, 31, and 72 had the highest average yields (10219, 9352, and 10263 kg/ha, respectively). (d) 2018 plots with locations of yield sampling points shown in yellow. Only points that are within plot boundaries and were not removed by the filtering procedure are shown. Plots 53, 91, and 92 had the lowest average yields (3456, 1859, and 3008 kg/ha, respectively), and plots 73, 74, and 83 had the highest average yields (9790, 9394, and 9179 kg/ha, respectively).

diameter 3× the swath width. If this point is not within one standard deviation of the local mean, exclude it.

5) Exclude points in step 4 that used less than 25% of the maximum possible number of points to calculate the local mean and standard deviation.

Field boundary points were removed because the edges of the field are often different from the rest of the field, due to soil compaction and animal interference. The 25% in step 5 was chosen based on trial and error, to ensure that there would be sufficient points to do the statistics without removing too many data points. This data cleaning procedure is modified from the approaches outlined by Kharel *et al.* [28] and Sudduth *et al.* [29], due to lacking some of the information used in those other approaches. Finally, yield mass for all points was calculated at 14% moisture content using the following equation:

$$\text{Wet Mass}_{14\%} = \frac{(\text{Wet Mass}_{X\%}) * (1 - X\%)}{(1 - 0.14)} \quad (1)$$

where $X\%$ refers to the original moisture content for the yield data point.

To find plot-average yield, cleaned yield data points falling within each pixel-based ROI were assigned to that plot, and the average wet mass at 14% moisture was calculated for each plot. Two 2019 plots containing fewer than 4 yield data points were excluded from the analysis, leaving 17 plots for VI-yield correlation in 2019 and 20 plots for VI-yield correlation in 2018. The 2018 and 2019 plot layouts and yield data points are shown in Fig. 1.

D. Preparing a VI Time-Series for VI-Yield Correlation

Because this experiment deals with temporally resampled data (detailed in Section II-F below), VI time-series must be smoothed and gap-filled before VI can be correlated with yield. Two methods for smoothing and gap-filling VI time-series are considered in this article: Shape model fitting and local fitting to a polynomial function.

A temporal shape model is a mathematical function that is fit to an image-derived quantity, such as a VI, over time. It may be used to smooth and fill gaps in noisy time-series data or to derive information about phenological transition timing. The asymmetric double sigmoid function, also called a double or piecewise logistic function, is a common function used for vegetation shape modeling. Researchers have used this function to monitor corn and soybean growth [30]–[32] and to predict cereal yield [8]. The functional form for the asymmetric double sigmoid function is given as follows:

$$V(t) = V_b + \frac{1}{2}V_a[\tanh(p*(t-D_i)) - \tanh(q*(t-D_d))] \tag{2}$$

where V_b is the background or baseline value, V_a is the amplitude, D_i and D_d represent the dates when the function is increasing or decreasing most rapidly, and p and q relate to the rate of increase or decrease in their respective segments. In addition to D_i and D_d, there are four derivable parameters that correspond to phenological transition dates. $D1$ and $D2$ represent the start and end dates of the period of rapid growth, and $D3$ and $D4$ represent the start and end of the period of rapid senescence. These four parameters can be found by finding the local maxima and minima of the function's second derivative, given as follows:

$$\begin{aligned} V''(t) = & -V_a[p^2\tanh(p*(t-D_i))\operatorname{sech}(p*(t-D_i))^2 \\ & - q^2\tanh(q*(t-D_d))\operatorname{sech}(q*(t-D_d))^2]. \end{aligned} \tag{3}$$

More details on the implementation of shape model fitting for these data can be found in the authors' previous article [32].

Instead of fitting a function to the entire time-series, which may prove difficult with data that is noisy or collected before growing season has ended, it is possible to smooth the time-series data using a local, moving filter. This article adapts the flexible fitting (Flexfit) method detailed by Gao *et al.* for this task [26]. Although Flexfit is similar to Savitzky–Golay filtering, which has been shown effective at smoothing VI time-series [33], it has a couple of additional capabilities: It can fill gaps in the data instead of just smoothing it and can be implemented in datasets that are not uniformly spaced. In this article, Flexfit was implemented as follows, using the polyfit function in MATLAB R2018b for the least-squares polynomial fitting step.

1) For each point in time that you wish to fit, find the 5 nearest points.
2) Perform least-squares fitting of a fourth-order polynomial on those 5 points.
3) Take the value of the polynomial at that point in time as the VI at that point.

It is possible to change the number of points or degree of polynomial used in the fitting, or to impose other restrictions on the fit.

Since variations in growing conditions cause plots to emerge on different days and mature at different rates, some researchers have found that it makes sense to use phenological transition times as a reference point (e.g., days after green-up, days before silking, etc.) rather than day of year [1]–[4], [34]–[36]. In this experiment, two such reference points were considered: Day of peak VI and green-up date.

Day of peak VI for each plot was found by searching for the maximum VI value reached by each plot. The day on which the maximum VI occurred was recorded unless it was on the last day of the time-series (suggesting that the crops may not have reached their peak VI value yet) or the maximum value occurred over three or more days (suggesting a possible bad fit). For time-series fit using the asymmetric double sigmoid function, the parameter D1 was used as a proxy for green-up date and was calculated for each plot as described previously. For time-series fit using Flexfit, the green-up date was calculated using the moving average convergence divergence (MACD) approach outlined by Gao *et al.* [26].

The MACD uses the difference between two exponential moving averages (EMA)—one calculated over a shorter period (a) and one over a longer period (b)—to identify new trends in a time-series. A signal line is an EMA of the MACD series for a different period (c). Although this approach was originally designed to monitor changes in stock prices, it was adapted by Gao *et al.* to detect corn and soybean green-up dates [26]. The MACD divergence, also called a histogram, for date t is defined by the following set of equations:

$$\begin{aligned} \text{MACD}_{\text{div}}(t) &= \text{MACD}(t) - \text{EMA}(\text{MACD}(t), c) \\ \text{MACD}(t) &= \text{EMA}(v(t), a) - \text{EMA}(v(t), n) \\ \text{EMA}(v(t), n) &= v(t)*k + \text{EMA}(v(t-1), n)*(1-k) \\ k &= 2.0/(n+1) \end{aligned} \tag{4}$$

where $v(t)$ is the time-series VI, EMA is the time-series exponential moving average, and n is the number of days used to compute EMA. EMA is a weighted moving average that gives more weight to recent observations. The computation of EMA starts from index $n+1$, with the first *EMA* at $t=n$ computed using a simple moving average (SMA) based on the beginning n points

$$\text{EMA}(v(n), n) = \text{SMA}(v(n), n) = \sum_{i=1}^{i=n} v(i)/n. \tag{5}$$

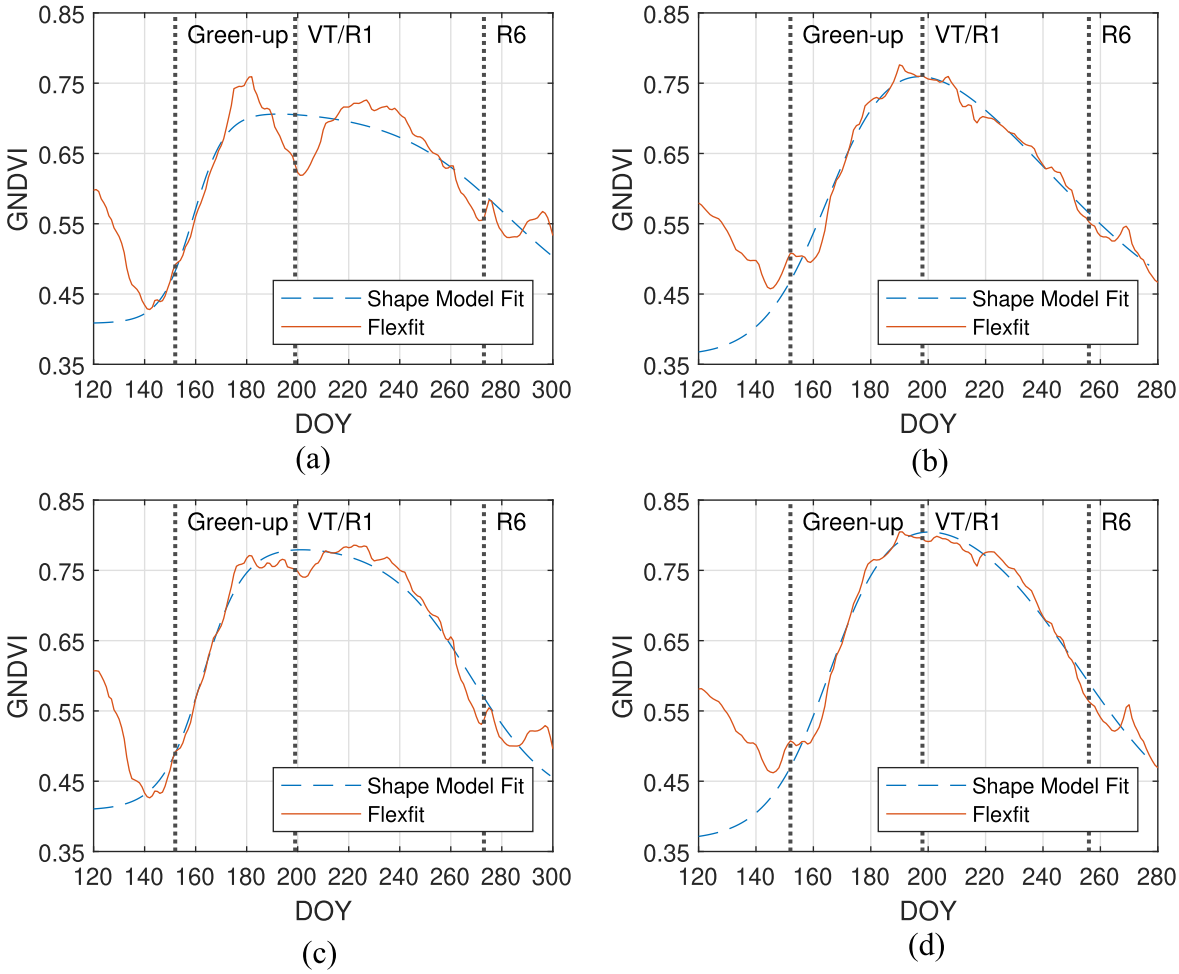

Fig. 2. Daily GNDVI time-series data shown after both smoothing methods. Vertical lines show the approximate times during the growing season when plants reached green-up, reproductive stages (VT/R1: Tassel and silk), and physiological maturity (R6). Shown for (a) a low-yield plot in 2018 (Plot 53), (b) a low-yield plot in 2019 (Plot 11), (c) a high-yield plot in 2018 (Plot 73), and (d) a high-yield plot in 2019 (Plot 23). Mid-summer drought in 2018 caused a large dip in GNDVI for nonirrigated plots (a) and a small dip in GNDVI for irrigated plots (c). Because Flexfit in these plots was performed on daily time-series data, it looks very similar to the nonsmoothed data.

Once the MACD divergence was calculated for an entire time-series, potential green-up events were found by looking for increasing trends of the time-series VI at date t that satisfied several threshold conditions, which are described in the article from which this approach was adapted [26].

Finally, the momentum (m) of these potential green-up events was calculated using the cumulative positive MACD between each of the potential green-up event and next green-up event (or the end of the time-series), divided by the number of days (npdays) of positive MACD after green-up

$$m(\text{greenup}) = \sum_{i=\text{greenup}}^{\text{next\_greenup}} \text{positive\_MACD}(i)/\text{npdays}. \quad (6)$$

Green-up events were kept if their momentum was greater than 0.01, they occurred within 20 d of the planting date, and they passed a final test: The simple moving average (SMA) of the VI time-series (v) over an n-day window should increase between the green-up date (used as the middle value of the SMA calculation) and the point n days after the green-up date. The equation for this VI-test is given as

$$\text{SMA}(v(\text{greenup}, n)) < \text{SMA}(v(\text{greenup} + n, n)). \quad (7)$$

This article used $a = 12$, $b = 20$, and $c = 15$ for the MACD divergence calculations and $n = 7$ d for the VI-test. While the values for a, b, and c were based on experimentation with different values, the various threshold values for green-up detection and the window size for the VI-test were taken from the article proposing this method [26].

Examples of smoothed GNDVI time-series data for low-yield and high-yield plots in 2018 and 2019 are shown in Fig. 2.

Finally, once plot-average VI time-series are smoothed, gap-filled, and temporally realigned at green-up, D1, or peak VI dates, plot-average VI for each day of the growing season can be correlated with plot-average yield using fitting to a linear or exponential equation. Linear least squares correlation was performed using the "poly1" fittype of the MATLAB fit function, and exponential correlation was performed using the "exp1" fittype. Default MATLAB settings were used to perform fitting. For exponential correlation, these included nonlinear least-squares

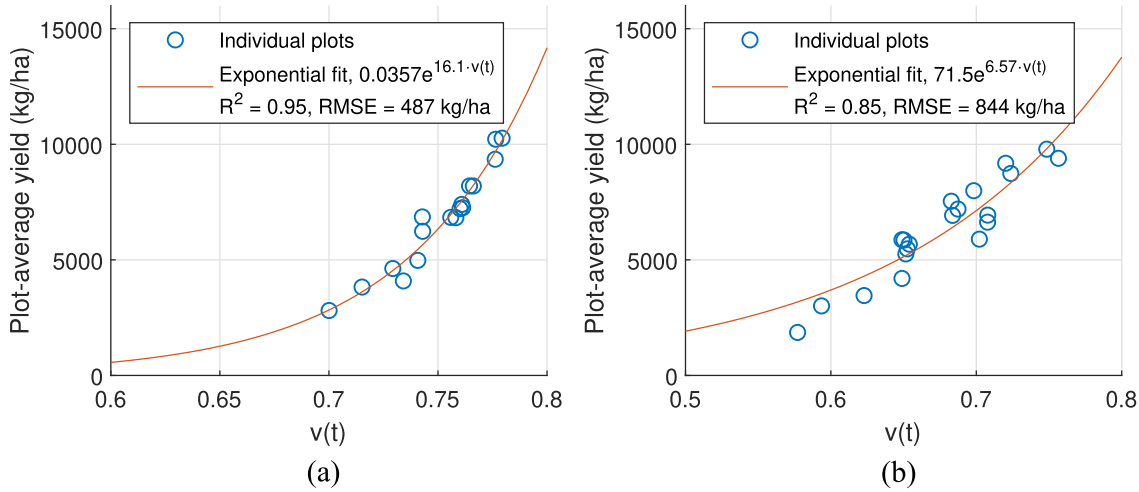

Fig. 3. Examples of exponential correlation performed after gap-filling and smoothing. (a) 2019 plot-average yield versus plot-average GNDVI 72 d after green-up, calculated after performing flexible fitting on daily GNDVI time-series data. (b) 2018 plot-average yield versus plot-average GNDVI 52 d after green-up, calculated after performing flexible fitting on daily GNDVI time-series data.

fitting using the trust-region algorithm with a maximum of 400 iterations used for the fit. The equation for the exponential function is given below

$$\text{yield} = a * e^{b*v(t)} \tag{8}$$

where a and b are constants determined by fitting, and v(t) is the time-series GNDVI after gap-filling and smoothing. Some examples of the exponential correlation are shown in Fig. 3.

E. Parameter Selection

Several initial experiments were performed to choose parameters for the temporal resampling experiments that are the main focus of this article. These included choosing a VI, choosing between linear and exponential correlation, choosing between temporal realignment at D1/green-up or day of peak VI, and choosing parameters for Flexfit and MACD green-up detection.

Eight different vegetation indices were tested on full, smoothed time-series data with both linear and exponential correlations. These indices were the enhanced vegetation index (EVI) [37], 2-band enhanced vegetation index (EVI2) [38], green chlorophyll index (GCI) [39], green normalized difference vegetation index (GNDVI) [39], normalized difference vegetation index (NDVI) [40], soil-adjusted vegetation index (SAVI) [41], wide dynamic range vegetation index (WDRVI, $\alpha = 0.1$) [42], and MODIS wide dynamic range vegetation index (WDRVI, $\alpha = 0.2$) [4]. In general, they all performed similarly. GNDVI was chosen for the temporal resampling experiments, as it performed well across multiple scenarios, but most of the other indices would have likely worked. The equation for GNDVI is given as

$$\text{GNDVI} = \frac{\rho_{\text{NIR}} - \rho_{\text{GREEN}}}{\rho_{\text{NIR}} + \rho_{\text{GREEN}}} \tag{9}$$

where ρ_{NIR} is the reflectance in the NIR wavelength band and ρ_{GREEN} is the reflectance in the green wavelength band.

Similarly, in initial experiments, both linear and exponential functions for VI-yield correlations were considered. Both correlation types exhibited similar behavior. In the 2019 data, which represented a more typical growing season, exponential correlations generally exhibited slightly higher R^2 values than linear correlations. Because of this, exponential function fitting was used for VI-yield correlation in the temporal resampling experiments, but linear fitting would have given similar results.

Temporal realignment at the day of peak GNDVI was considered in initial experiments. Although this method performed similarly to realignment at D1 or green-up for time-series ending late in the growing season, it was not usable for time-series ending around or before the day of peak VI.

Second-order, third-order, and fourth-order polynomials were considered for use in the Flexfit algorithm. In order to choose, VI time-series data were resampled to different revisit intervals and gap-filled and smoothed using the Flexfit method with second, third, and fourth-order polynomial functions. Root mean square error (RMSE) is calculated between the Flexfit-generated time-series and original data. For all revisit intervals, time-series that were gap-filled and smoothed using fourth-order polynomials were the closest to the original time-series data, with the lowest RMSE.

To choose values of a, b, and c for MACD divergence calculation, many different combinations were tested. Values of a ranged from 5–15, values of b ranged from 10–20, and values of c ranged from 5–15. Using the largest values for a, b, and c resulted in green-up dates detected 3–4 d later than those calculated using the smallest values of those parameters, but relationships between green-up dates for different plots (i.e., green-up for plot A occurs one day before green-up for plot B) were preserved across different a–b–c combinations. Because later-detected green-ups were more likely to pass the VI-test, the relatively large values of $a = 12$, $b = 20$, and $c = 15$ were chosen for this experiment.

F. Temporal Resampling Experiments

Daily plot-average GNDVI time-series for 20 different corn plots in 2018 and 17 different corn plots in 2019 (shown in Fig. 1) were resampled to different revisit intervals, which

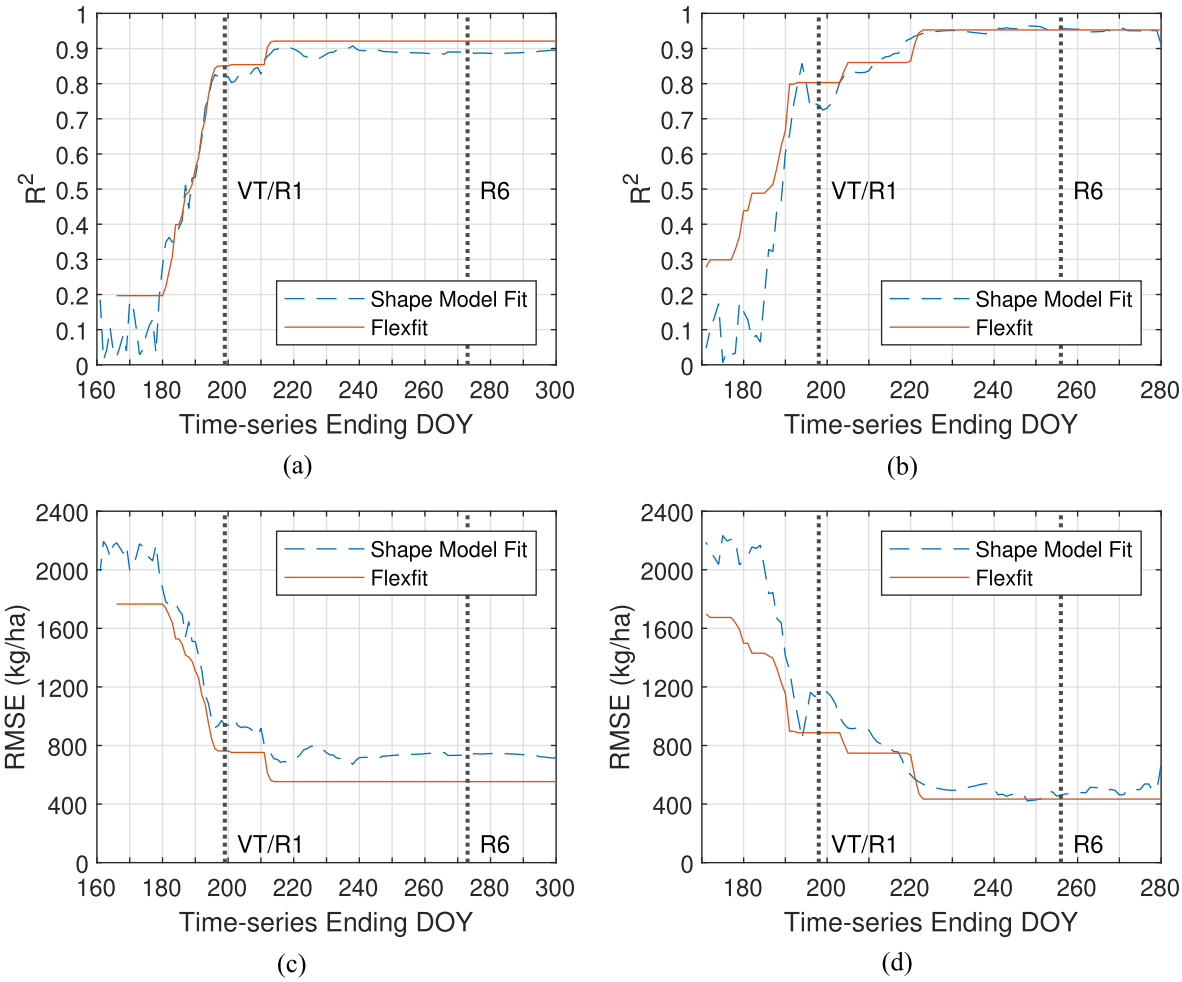

Fig. 4. Highest-possible R^2 and corresponding RMSE values for GNDVI-yield exponential correlation for daily time-series data, shown as a function of time-series end date. Vertical lines show the approximate times during the growing season when plants reached the reproductive stages (VT/R1: Tassel and silk) and when plants reached physiological maturity (R6). (a) 2018 R^2 values. (b) 2019 R^2 values. (c) 2018 RMSE values. (d) 2019 RMSE values.

ranged from 1 to 30 d between successive images. Resampling was performed as follows. Starting with the first day of the time-series, sequences of dates were created that were defined by revisit interval and offset from the starting date (ranging from 0—starting on DOY 1—to revisit interval minus 1). For example, there were two 2-d sequences given by (1, 3, 5, . . .) and (2, 4, 6,. . .), three 3-d sequences, and so on. The plot-average GNDVI at these dates were used as the resampled time-series data for the experiments.

After resampling, plot-average VI time-series were smoothed and gap-filled according to one of two methods: Fitting the data to an asymmetric double sigmoid function, or local polynomial fitting with Flexfit. They were realigned at D1 (asymmetric double sigmoid function fit) or green-up (Flexfit). Plot-average yield after realignment was correlated with plot-average GNDVI using exponential function fitting, and goodness-of-fit results (R^2 and RMSE) as well as day of best correlation (in relation to D1 or green-up) were recorded. Finally, data points were removed from the end of the time-series and the process of smoothing and gap-filling, realignment, and yield correlation was repeated. For the 2019 data, time-series end dates ranged from DOY 280 (3 d after harvest) to DOY 171 (roughly 20 d before peak GNDVI). For the 2018 data, time-series end dates ranged from DOY 300 (1 d after harvest) to DOY 161 (roughly 20 d before the first peak in GNDVI).

The goal of these experiments was to understand which fitting methods were most accurate for VI-yield prediction, as well as understanding how these methods were affected by increasing the time between subsequent images or by attempting to predict yield early in the growing season.

III. Results

The following sections describe the results of different resampling experiments. These include comparisons between different fitting methods, and effects of image frequency and time-series end date on yield prediction accuracy.

A. *Effects of Time-Series End Date on VI-Yield Correlation*

Fig. 4 shows the R^2 and RMSE values for GNDVI-yield correlations as a function of time-series end date, looking only

TABLE I
TIME-SERIES END DATES AT WHICH R^2 FOR GNDVI-YIELD CORRELATIONS REACH THEIR PEAK VALUES AND RMSE VALUES ARE MINIMIZED, FOR DIFFERENT FITTING METHODS APPLIED TO DAILY TIME-SERIES DATA*

		Best Correlation				Second-Best Correlation			
Year	Fitting Method	End DOY	Days after Green-Up	R^2	RMSE (kg/ha)	End DOY	Days after Green-Up	R^2	RMSE (kg/ha)
2019	Flexfit	223	72	0.95	486	205	54	0.86	833
2019	Shape Model Fit	223	58-64	0.95 ± 0.01	494 ± 38	N/A			
2018	Flexfit	214	65	0.92	620	201	52	0.85	844
2018	Shape Model Fit	214	59-84	0.89 ± 0.01	733 ± 23	N/A			

*Quantities for shape model fitting are presented as an average of the relatively flat portions of the curve in Fig. 4, i.e., DOY 214 and later in 2018 and DOY 223 and later in 2019.

at fitting performed on daily image time-series data, and Table I shows the days, R^2 values, and RMSE values of the best and second-best GNDVI-yield correlation for different fitting methods and years. In Table I, "End DOY" shows the earliest time-series end dates for each year at which GNDVI-yield correlation R^2 reach their peak values, while "Days after Green-Up" shows the actual days when GNDVI-yield correlation is highest. For shape model fitting, these quantities do not always match, as extra data points at the end of the time-series can be helpful for getting a good curve fit around the day of best correlation. Finally, quantities for shape model fitting are presented as a range of values over the flat portions of the curve, i.e., DOY 214 and later in 2018 and DOY 223 and later in 2019. This was done to account for fluctuations in the shape model fitting process. Because the shape model fits the entire time-series, it gives different values for day of best correlation depending on time-series end date.

For both fitting methods, R^2 correlations are generally higher and RMSE values are generally lower for later time-series end dates. In the 2018 Flexfit data, distinct drop-offs in R^2 correlation occur around DOY 214 and DOY 197. In the 2019 Flexfit data, drop-offs in R^2 correlation occur around DOY 223, DOY 205, and DOY 193. The 2018 and 2019 shape model fitting data show similar decline in R^2 correlation with earlier time-series end dates, but changes are more noisy and less discrete than in the Flexfit data. Because of this, days of second-best correlation have not been reported in Table I for shape model fitting, although it can be seen in Fig. 4 that the sharpest drop-offs in R^2 for both years and both fitting methods occur around or slightly before the start of the reproductive stages.

As will be discussed in the following section, time-series at different revisit intervals generally follow similar trends, but with noisier and slightly lower R^2 values from correlation.

B. *Effects of Revisit Interval on VI-Yield Correlation*

Fig. 5 shows the R^2 of GNDVI-yield correlation for several different revisit intervals (1, 10, 20, and 30 d) as a function of time-series end date. Two dates are marked on the plots: T1 (DOY 197 in 2018 and DOY 193 in 2019) and T2 (DOY 214 in 2018 and DOY 223 in 2019). T1 is the earliest date of stable GNDVI-yield correlation; time-series data ending before T1 drop rapidly in R^2 correlation, as discussed in Section III-A. T2 is the date of peak GNDVI-yield correlation; time-series data ending on or after T2 achieve maximum R^2 correlation for the case of daily revisit, as discussed in Section III-A. For the 2019 data, and to a lesser extent the 2018 data, the variability in goodness of correlation (as measured by R^2) increases with increasing revisit interval. Although RMSE is not shown in this figure, it follows similar trends of increasing variability with increasing revisit interval. The regularity of the R^2 oscillations visible after T2 in Figs. 5(b) and (d) suggests that some images within the 2019 dataset were more important to yield correlation than others—perhaps there are a few misleading images that skew the results when they are sampled without other points around them. Resampling the data at regular intervals ensures that any particularly "good" or "bad" points will be used in the correlation at regularly spaced time-series end dates.

Fig. 6 further explores the R^2 values for GNDVI-yield correlation performed after the day of peak correlation (T2). On the left, the average of R^2 values for time-series end dates ranging from T2 to harvest are shown for each revisit interval. On the right, the lowest-occurring R^2 value for each revisit interval within that same range of dates is shown. For example, in Fig. 5(a), it can be seen that R^2 for 2018 time-series data sampled to 30-d revisit intervals before being smoothed by shape model fitting reaches an approximate minimum value of 0.6 around DOY 220. In Fig. 6(b), that minimum R^2 value of 0.6 is marked on the plot for the 2018 shape model fitting data at the 30-d revisit interval.

In general, the mean R^2 values over this date range decrease fairly slowly with increasing revisit interval. Mean R^2 values for 2019 data, which were higher than those for 2018 data when daily imagery is used, only decrease by 0.05 or more when sampled from 1 to 22-d revisit intervals (shape model fitting) or from 1 to 30-d revisit intervals (Flexfit). Mean R^2 values for 2018 data never decrease by 0.05 or more, even when sampled from 1 to 30-d revisit intervals. For time-series data at large revisit intervals ($\geq$20 d), mean Flexfit R^2 is higher than mean shape model fitting R^2 for both years of data. R^2 values for both years of shape model fitting also reach lower minimum values at large revisit intervals, which suggests that shape model fitting might produce more variable results for sparse image time-series.

Fig. 7 looks at the differences between R^2 values for daily time-series data and R^2 values for data at other revisit intervals, shown for time-series data ending before the day of peak correlation. Best-correlation R^2 values from GNDVI-yield correlation for daily time-series data, shown previously in Fig. 4, served as a baseline from which R^2 values for other revisit intervals were measured. Unlike in Fig. 6, statistics for Fig. 7 were calculated for time-series end dates between the earliest day

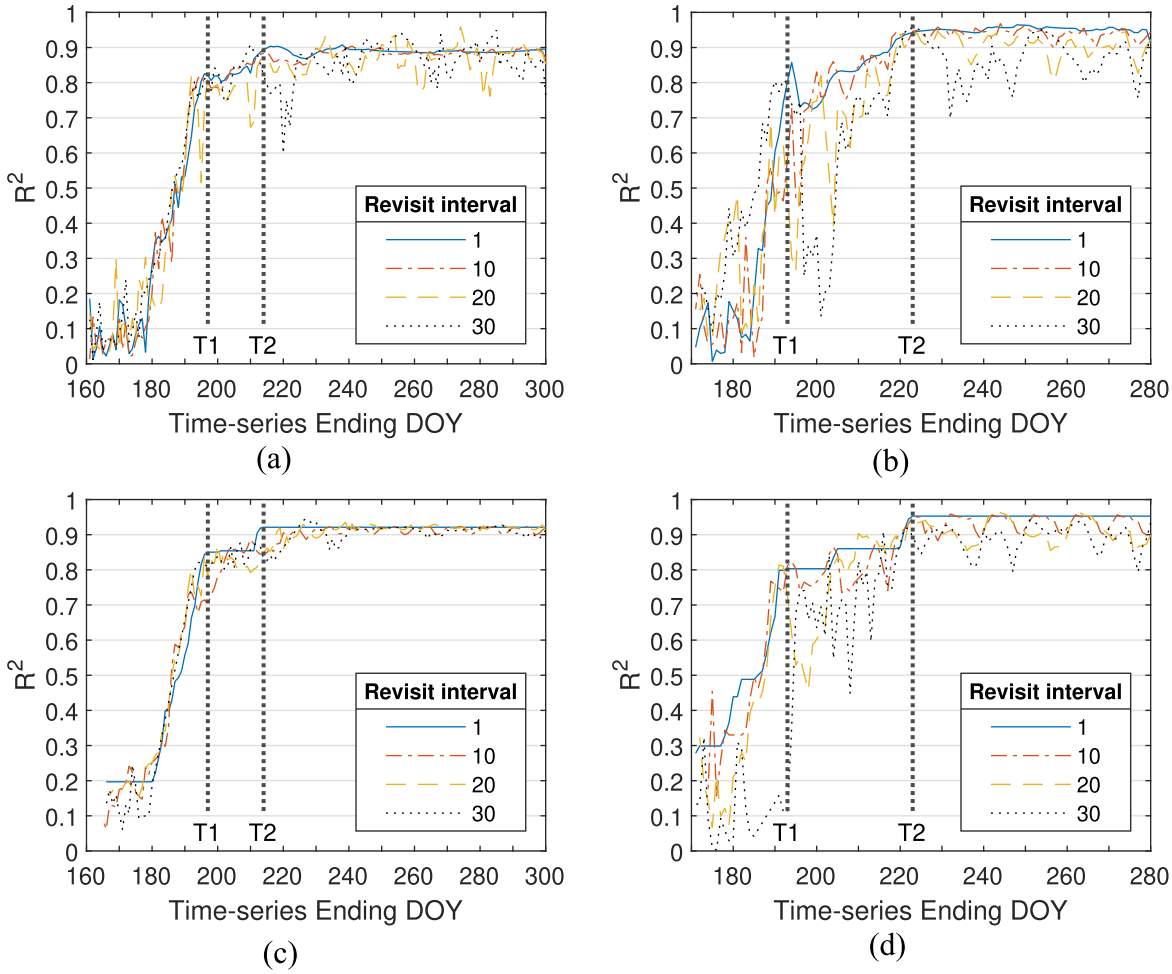

Fig. 5. R^2 of GNDVI-yield correlation for several different revisit intervals. T1 marks the end date before which sharp drop-offs in GNDVI-yield correlation occur (DOY 197 in 2018, DOY 193 in 2019). T2 marks the end date after which peak correlation occurs (DOY 214 in 2018, DOY 223 in 2019). (a) 2018 shape model fitting data. (b) 2019 shape model fitting data. (c) 2018 flexfit data. (d) 2019 flexfit data.

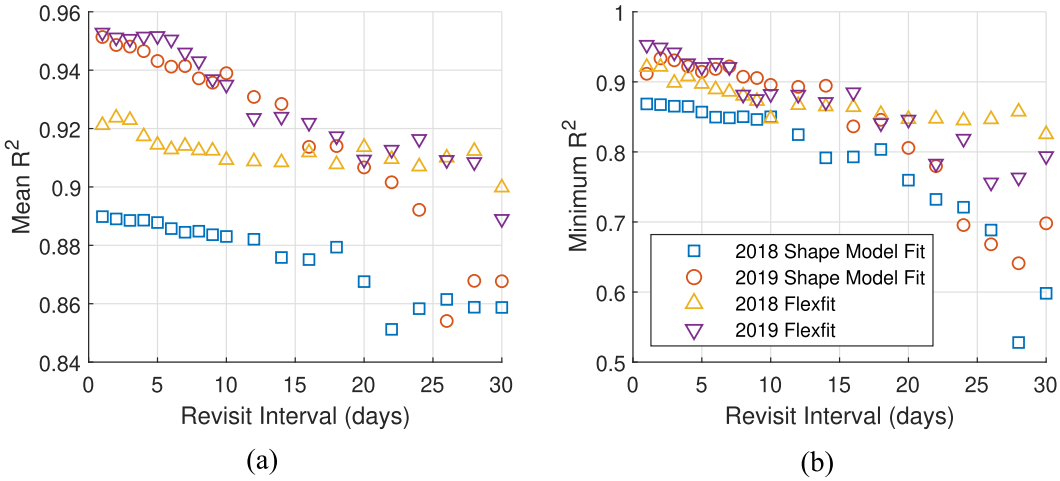

Fig. 6. Mean and minimum R^2, calculated over time-series data ending after the day of peak GNDVI-yield correlation (T2 in Fig. 5), shown as a function of revisit interval. Statistics for 2018 data were calculated over time-series end DOY 214-300, and statistics for 2019 data were calculated over time-series end DOY 223-280. (a) Mean value of R^2 for time-series ending after the day of peak correlation. (b) Lowest value of R^2 for time-series ending after the day of peak correlation.

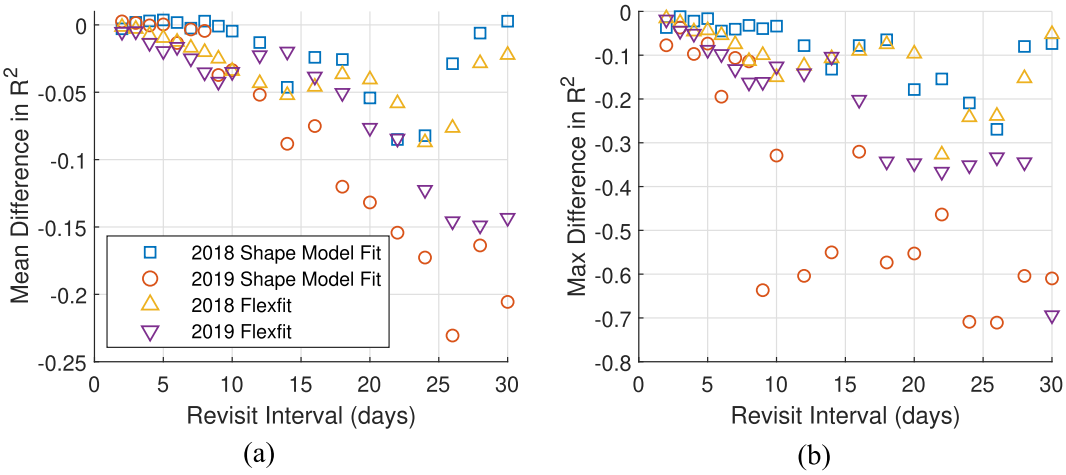

Fig. 7. Comparison between R^2 values calculated at 1-d revisit intervals and values calculated at other intervals, for time-series data ending after the date at which sharp drop-offs in GNDVI-yield correlation occur (T1 in Fig. 5) and before the day of peak GNDVI-yield correlation (T2), shown as a function of revisit interval. Statistics for 2018 data were calculated over time-series end DOY 197-213, and statistics for 2019 data were calculated over time-series end DOY 193-222. (a) Mean difference between R^2 for GNDVI-yield correlations calculated at 1-d revisit intervals and R^2 for GNDVI-yield correlations at other revisit intervals. (b) Largest difference between R^2 for GNDVI-yield correlations calculated at 1-d revisit intervals and R^2 for GNDVI-yield correlations at other revisit intervals.

of stable GNDVI-yield correlation (T1) and the day of peak correlation (T2), in order to gain an idea of how increases in revisit interval affect yield correlation earlier in the growing season. On the left, the mean differences between R^2 values for daily revisit and R^2 values for other revisit intervals, for all time-series ending between T1 and T2, are shown for each revisit interval. On the right, the maximum difference between daily R^2 and R^2 for other intervals is shown. Statistics were presented as differences from 1-d R^2 rather than R^2 values because GNDVI-yield correlations for time-series ending before the day of peak correlation are not constant with respect to time-series end date.

In general, R^2 values over this date range decrease with increasing revisit interval, with 2019 data following this trend more strongly at larger revisit intervals. Mean R^2 values first decrease by 0.05 or more when sampled from 1 to 12-d revisit intervals (2019 shape model fitting), 1 to 14-d revisit intervals (2018 Flexfit and 2018 shape model fitting), and 1 to 18-d revisit intervals (2019 Flexfit). Mean R^2 values for 2019 data first decrease by 0.10 or more when sampled from 1 to 18-d revisit intervals (2019 shape model fitting) or from 1 to 24-d revisit intervals (2019 Flexfit). Mean R^2 values for 2018 data never decrease by 0.10 or more. These are sharper rates of decrease than those shown in Fig. 6, indicating that time-series ending earlier than the day of best GNDVI-yield correlation may be more subject to variability in goodness of correlation than time-series ending later. Some evidence of this can be seen in Fig. 5 - R^2 for 2019 time-series ending between T1 and T2 diverge much more strongly from 1-d R^2 than R^2 for time-series ending after T2.

Fig. 8 shows the mean RMSE for GNDVI-yield correlations performed after the day of peak correlation (left) and the mean difference between 1-d RMSE and RMSE for other intervals, for time-series ending between the earliest day of stable GNDVI-yield correlation and the day of peak correlation (right). RMSE data for both of the date ranges behave similarly to R^2 over the same ranges.

There is an interesting difference between the overall results for the 2018 data, which were less strongly affected by resampling, and the results from the 2019 data, which showed larger decreases in GNDVI-yield correlation R^2 with increased revisit interval. There are multiple factors that could contribute to this phenomenon. First, starting R^2 values for GNDVI-yield correlation were slightly higher for the 2019 data than they were for the 2018 data, meaning that they could decrease more than 2018 correlations while maintaining similar goodness of fit. Second, differences in growing conditions between the two years affected the accuracy of the gap-filling and curve-fitting processes, which in turn may have affected the yield correlation results. Because the 2019 data represent a more typical growing season, without a mid-season drought causing a noticeable dip in vegetation health, the results from the 2019 data may be more representative of the typical effects of revisit interval on goodness of yield prediction. However, more data are needed to fully understand why these differences in results exist.

C. *Shape Model Fitting Versus Flexfit*

Both gap-filling and smoothing methods considered in this study provided daily GNDVI time-series data that could be correlated highly with yield, but it is worth exploring the ways in which they differed.

Gap-filling and smoothing the time-series data using different methods resulted in slightly different dates detected for phenological transition points, as shown in Table II. In general, D1 and green-up dates were similar. For most of the plots in 2018, green-up occurred around DOY 146-149 and D1 occurred around DOY 149-154. For most of the plots in 2019, green-up occurred around DOY 150-151 and D1 occurred around DOY 151-154. It is worth noting that the green-up date was affected by the MACD parameters chosen, as discussed in Section II-E. The day of peak GNDVI, calculated after gap-filling and smoothing, differed between methods. For the plots in 2018, a drought caused a dip in mid-season GNDVI values,

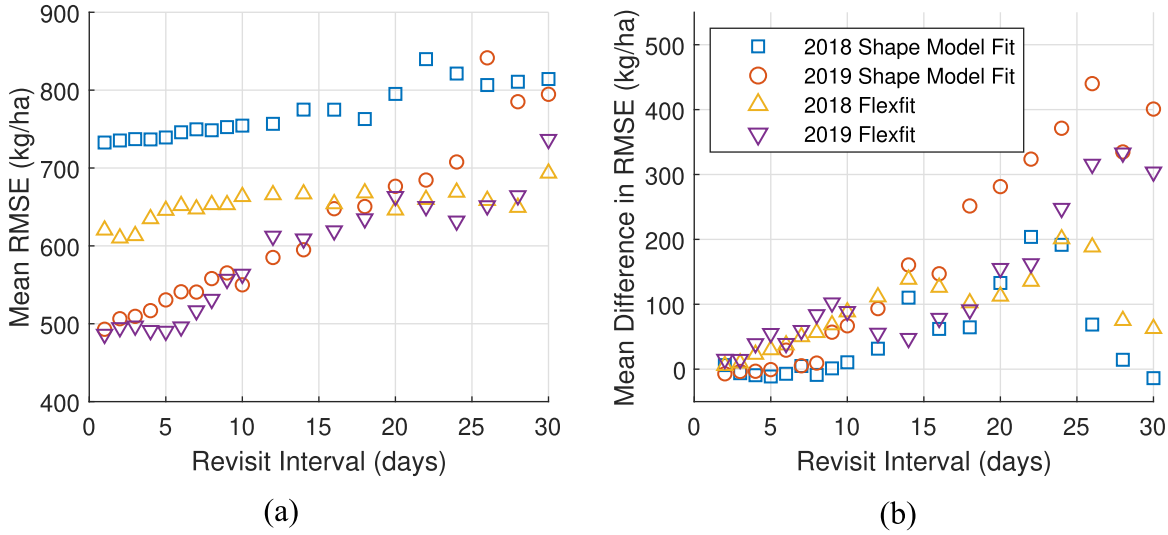

Fig. 8. (a) Mean value of RMSE for time-series ending after the day of peak correlation (T2), shown as a function of revisit interval. (b) Mean difference between RMSE for GNDVI-yield correlations calculated at 1-d revisit intervals and RMSE for GNDVI-yield correlations at other revisit intervals, calculated over time-series data ending between T1 and T2.

TABLE II
DAY OF GREEN-UP OR D1 AND PEAK GNDVI, BASED ON COMPLETE 1-D TIME-SERIES DATA

Year	Gap-Filling & Smoothing Method	Green-up DOY	Peak GNDVI DOY
2019	Flexfit	150±0	191±2
2019	Shape Model Fit	152±1	198±2
2018	Flexfit	148±1	180±2, 224±3
2018	Shape Model Fit	152±2	199±4

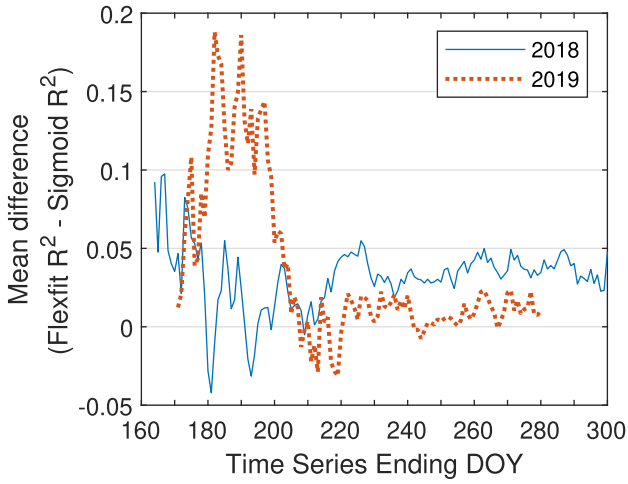

Fig. 9. Mean difference between R^2 for GNDVI-yield correlations performed after flexible fitting and R^2 for GNDVI-yield correlations performed after shape model fitting, shown as a function of time-series end date.

resulting in two GNDVI peaks for most plots. Peak GNDVI for 2018 plots after Flexfit occurred at either the first peak, around DOY 180, or the second peak, around DOY 222-227, depending on plot and on time-series end date. Peak GNDVI after shape model fitting occurred somewhere between these two peaks, around DOY 193-206, with peak values for most plots around DOY 199. Although day of peak GNDVI was not used in this experiment, these calculation differences could prove relevant to other researchers wishing to use one of these fitting methods for phenology detection or late-season yield prediction.

As shown in the previous sections, goodness of fit for both fitting methods exhibit similar patterns as a function of time-series end date, with R^2 values for both fitting methods first beginning to decrease around DOY 223 (2019) or 214 (2018) and then more sharply around DOY 190-200 (both years), and RMSE increasing at those same DOY. Specific comparisons between Flexfit and shape model fitting R^2 are shown as a function of time-series end date in Fig. 9.

For the data collected in 2018, R^2 from GNDVI-yield correlation after Flexfit were on average higher than R^2 after shape model fitting for most time-series end dates, as can be seen in Fig. 9—the mean difference between Flexfit R^2 and shape model fit R^2 is greater than zero in almost all cases. Many of these differences in R^2 were within one standard deviation, although mean Flexfit R^2 for time-series ending on DOY 218 or later were more than one standard deviation above R^2 from shape model fitting.

For data collected in 2019, R^2 from GNDVI-yield correlation after Flexfit versus shape model fitting methods were similar at time-series end dates after DOY 210, as can be seen in Fig. 9—the mean difference between Flexfit R^2 and shape model fit R^2 oscillates near zero. For earlier time-series end dates, however, time-series smoothed and gap-filled using the Flexfit method had a slightly higher R^2 for VI-yield correlation than time-series smoothed and gap-filled by fitting to the asymmetric double sigmoid function. These differences in R^2 were within one standard deviation.

As shown in Fig. 6 and discussed in Section III-B, R^2 from GNDVI-yield correlation after Flexfit were similar to R^2 from GNDVI-yield correlation after shape model fitting for 2019 data

at revisit intervals ≤ 20 d, and higher than R^2 from GNDVI-yield correlation after shape model fitting for all 2018 data and for 2019 data at revisit intervals > 20 d.

For the 2018 data, it is likely that Flexfit outperformed shape model fitting because the irregularities in the growing season meant that the data fit less well to the asymmetric double sigmoid function. For the 2019 data, which represented a more typical growing season, it is likely that Flexfit outperformed shape model fitting only for earlier time-series end dates because there was not enough data present to accurately fit the entire asymmetric double sigmoid function. Flexfit is less dependent on complete or predictable data because it fits each piece of the time-series locally.

IV. Discussion

A. Effects of Time-Series End Date on VI-Yield Correlation

As expected, yield correlation with GNDVI is higher later in the growing season. For daily GNDVI time-series smoothed with Flexfit, the yield is most highly correlated with GNDVI at 72 d after green-up in 2019 ($R^2 = 0.95$) and 65 d after green-up in 2018 ($R^2 = 0.92$). For daily time-series smoothed with asymmetric double sigmoid function fitting, the yield is most highly correlated with GNDVI around 58–64 d after D1 in 2019 ($R^2 = 0.95 \pm 0.01$) and 59–84 d after D1 in 2018 ($R^2 = 0.89 \pm 0.01$).

These findings are somewhat consistent with prior work by Shanahan *et al.* and Guindin-Garcia, who found that GNDVI and WDRVI around the mid-grain filling period (past the peak VI, in the middle of the reproductive growth stages) was most highly correlated with maize yield [2], [36], and Bolton and Friedl, who found that the best correlations between vegetation indices and yield were 65–75 d after green-up (calculated using shape model fitting) for maize [1]. The slight differences between the 2019 shape model fitting results and Bolton and Friedl's results may be partially explained by the use of exponential correlation instead of linear; initial experiments with this dataset using linear correlation resulted in a day of best correlation between 65 and 75 d after D1. The broad range of days of best correlation in the 2018 shape model fitting results may be caused by the atypical mid-season dip in GNDVI seen in many of the plots.

For daily GNDVI time-series smoothed with Flexfit ending before the day of best correlation (DOY 223 in 2019 or DOY 214 in 2018), the next-best yield correlation occurred at 54 d after green-up in 2019 ($R^2 = 0.86$) and 52 d after green-up in 2018 ($R^2 = 0.85$). The 2019 Flexfit data also had a third-best day of correlation 42 d after green-up ($R^2 = 0.80$). Both the second-best correlation in 2018 and third-best correlation in 2019 occurred around the time of peak GNDVI for this data. Many other researchers have found strong VI-yield correlations around the silking stage in maize, which corresponds roughly to this portion of the VI time-series [3], [4], [34], [35]. For daily Flexfit-smoothed time-series data ending before DOY 193 in 2019 or DOY 197 in 2018, the R^2 correlation drops rapidly to values below 0.50. Daily sigmoid-fit time-series data follows similar trends. The trends for other revisit intervals are similar but noisier, as will be discussed in the following section.

These findings suggest that maize yield can be most accurately predicted from GNDVI around or after the peak in the time-series, which corresponds to the start of the maize reproductive growth stages.

B. Effects of Revisit Interval on VI-Yield Correlation

As discussed in Section III-B, increasing the amount of time between subsequent images in the time-series caused greater fluctuations in the goodness of fit for GNDVI-yield correlations.

For late-ending time-series data, accuracy of yield correlation decreases relatively slowly as a function of increasing revisit interval. Taking 2019 Flexfit data as an example (chosen because 2019 represented a more typical growing season and Flexfit performed similarly to or better than shape model fitting in most scenarios, as discussed in Section III-C), one image every 18 d may produce an R^2 value for GNDVI-yield correlation that is 0.10 less than the R^2 for the same dataset at daily revisit, and will more likely produce an R^2 value that is between 0.01 and 0.06 less. One image every 22 d may produce an R^2 value that is 0.15 less than the R^2 for the same dataset at daily revisit, and will more likely produce an R^2 value that is between 0 and 0.08 less. These differences are relatively small compared to the drop in correlation between late-ending time-series and earlier-ending time-series; however, late-ending time-series data must be sampled from 1 to 18-d intervals before the lowest possible value of R^2 is lower than the highest value of R^2 for daily time-series data ending before DOY 220 ($R^2 = 0.86$). The mean value of R^2 for late-ending time-series data never goes below this value, even when sampled from 1 to 30-d intervals.

For yield correlation earlier in the growing season (starting around the time of peak GNDVI), accuracy of yield correlation decreases more rapidly as a function of increasing revisit interval. One image every 6 d may produce an R^2 value for GNDVI-yield correlation that is 0.10 less than the R^2 for the same dataset at daily revisit, and will more likely produce an R^2 value that is between 0 and 0.05 less. One image every 8 d may produce an R^2 value for GNDVI-yield correlation that is 0.15 less than the R^2 for the same dataset at daily revisit, and will more likely produce an R^2 value that is between 0 and 0.08 less. One image every 16 d may produce an R^2 value that is 0.20 less than the R^2 for the same dataset at daily revisit, and will more likely produce an R^2 value that is between 0 and 0.10 less.

Using imagery that is high in both spatial resolution and radiometric quality may also reduce the need for frequent imagery. Mean and lowest late-season R^2 for time-series data sampled from 1 to 28-day revisit intervals are greater than the R^2 values achieved in similar studies using medium spatial resolution imagery (30 m) or high spatial resolution imagery (3 m) of lower radiometric quality than the L3H data product (PlanetScope surface reflectance imagery) [10], [24], [43]. Mean late-season R^2 for time-series data sampled from 1 to 30-d revisit intervals, and lowest late-season R^2 values for time-series data sampled from 1 to 16-d revisit intervals are higher than best-fit R^2 obtained by several comparable studies using coarse spatial resolution MODIS imagery (250–1000 m) to study maize yield at the United States of America county level [1], [3], [4], [43].

At least one MODIS-based study did attain comparable R^2 values for MODIS-derived LAI-yield correlation ($R^2 = 0.77$, 0.86, and 0.94) [2]. While these differences are likely due in part to the small size of this study, as well as between-study differences in spatial aggregation of image and yield data [10], they may also indicate that imagery that is high in both spatial and radiometric resolution can achieve higher yield correlation at less frequent intervals than imagery that is lacking in one of these areas.

These findings suggest that while image frequency does affect yield correlation accuracy, the strength of this effect may depend on factors like time-series end date, image resolution, and image quality.

C. Recommendations and Future Work

Based on these findings, any of the explored methods for VI-yield correlation perform well for healthy maize at later time-series end dates, but gap-filling and smoothing time-series data with Flexfit and then realigning that data at the day of green-up results in higher correlations for data that is atypical, early in the growing season, or collected with more than 20 d between subsequent images.

For late-season yield estimation using high-quality, high-resolution satellite imagery, one image every 30 d may produce reasonably high GNDVI-yield correlation accuracy ($R^2 > 0.75$). For accurate yield correlation earlier in the growing season, the requirements are more strict. One image every 16 d might produce a reasonably high GDNVI-yield correlation accuracy, but one image every 6–8 d has less chance of producing a poor outcome.

The need for imagery at a specific interval (e.g., every 6–8 d for early-season maize yield prediction, or every 30 d for late-season maize yield prediction) is not as simple as having a satellite with that same overpass frequency. Cloud contamination is common in satellite imagery, and limits the availability of usable imagery. The findings of one study focused primarily on the eastern USA suggest that daily satellite imagery is needed in order to ensure at least one clear view a week, 2-d revisit is needed to ensure biweekly clear views, and 4-d revisit is needed to ensure monthly clear views [44]. A global analysis of PlanetScope imagery, which has an overpass frequency of 1–2 d for most parts of the world, gave slightly more optimistic numbers. They found that there is an average global probability of 0.84 of there being at least one cloud-free PlanetScope observation in every 5-d period, and an average global probability of 0.92 of there being at least one cloud-free PlanetScope observation in every 10-d period [45]. Of course, these probabilities vary across different locations and times of year. PlanetScope surface reflectance imagery over the Beltsville site in 2018 was found to have an average revisit interval of 1 image every 3 d, but there was a 20-d gap in coverage during the month of September [32].

Given the constraints on image data collection posed by cloud cover, the authors recommend a very high overpass frequency for future Landsat systems: An overpass frequency of 1 or 2 d would ensure the 1–2 week revisit recommended for accurate yield correlation earlier in the growing season, and an overpass frequency of up to 4 d would ensure a monthly revisit, which was shown to produce reasonably high late-season GNDVI-yield correlations.

In the future, the authors would like to add to the robustness of these results by collecting the same type of data over more years and fields. Because this study is small, covering a small site and a single crop (maize) over two growing seasons, some of the current results may not be applicable to other crops, locations, and growing conditions. Repeating this experiment with other high spatial and temporal resolution image sources, such as VENμS imagery, would also help in understanding how small differences in spectral, spatial, and temporal resolutions affect VI-yield correlation accuracy. Finally, repeating the analysis with nonuniform revisit intervals would better reflect the reality that cloud cover and other atmospheric conditions limit image availability for nonharmonized products.

V. Conclusion

In this article, we explored the effects of time-series end date and imaging frequency on our ability to correlate VI with maize yield, using daily, high-resolution (3-m GSD) multispectral satellite imagery. This study adds to the growing body of research on the use of Cubesats and harmonized sensor data for crop yield prediction, compares multiple approaches for gap-filling and detecting green-up dates in VI time-series (including new methodologies like Flexfit and MACD-based green-up detection), and contributes to ongoing research into temporal imaging requirements for agricultural monitoring by examining the relationship between yield correlation accuracy and satellite revisit interval.

We found that realigning plot-average GNDVI time-series at their respective green-up dates before performing VI-yield correlations gave the most consistent results across different time-series end dates. We considered two different methods of gap-filling and smoothing GNDVI time-series data: Fitting the data to a temporal shape model, or performing local fitting with the Flexfit method. Both methods yielded similarly high R^2 values for GNDVI-yield correlations performed later in the growing season (around or after DOY 223 in 2019, which was roughly 72 d after green-up, or DOY 214 in 2018, which was roughly 65 d after green-up). Both methods yielded low R^2 values for GNDVI-yield correlations performed early in the growing season (prior to DOY 193 in 2019 or DOY 197 in 2018, which corresponded with the silking stage of maize growth), although Flexfit correlations were slightly higher. The mean R^2 from VI-yield correlation decreased with increasing revisit interval, and the variability in R^2 from VI-yield correlation increased with increasing revisit interval. The 2019 data demonstrated these trends more strongly than the 2018 data, and time-series ending earlier in the growing season demonstrated these trends more strongly than time-series ending later in the growing season. These findings suggest that although it is possible to obtain a high correlation between GNDVI and yield from infrequent satellite imagery, the chances of a poor correlation increase with increasing revisit interval or for correlation performed earlier in the growing season.

Finally, we discussed these results within the context of previous research into maize yield correlation and prediction using satellite imagery, and provided recommendations for optimal methodology and optimal satellite overpass frequency (1–4 d revisit) based on our findings.

ACKNOWLEDGMENT

The authors would like to thank Dr. R. Houborg of Planet Labs, Inc. (San Francisco, CA, USA) for providing the imagery used in this study. The authors would also like to thank W. Dulaney and A. J. Stern of the USDA for providing filtered yield data for the 2019 plots and describing the filtering process so that the authors could implement it on the 2018 data.

REFERENCES

[1] D. K. Bolton and M. A. Friedl, "Forecasting crop yield using remotely sensed vegetation indices and crop phenology metrics," *Agricultural Forest Meteorol.*, vol. 173, pp. 74–84, May 2013.

[2] N. Guindin-Garcia, "Estimating maize grain yield from crop biophysical parameters using remote sensing," Ph.D. dissertation, Graduate College, Univ. Nebraska-Lincoln, Lincoln, NE, USA, 2010.

[3] D. M. Johnson, "An assessment of pre- and within-season remotely sensed variables for forecasting corn and soybean yields in the United States," *Remote Sens. Environ.*, vol. 141, pp. 116–128, Feb. 2014.

[4] T. Sakamoto, A. A. Gitelson, and T. J. Arkebauer, "MODIS-based corn grain yield estimation model incorporating crop phenology information," *Remote Sens. Environ.*, vol. 131, pp. 215–231, Apr. 2013.

[5] M. Battude *et al.*, "Estimating maize biomass and yield over large areas using high spatial and temporal resolution Sentinel-2 like remote sensing data," *Remote Sens. Environ.*, vol. 184, pp. 668–681, Oct. 2016.

[6] M. Burke and D. B. Lobell, "Satellite-based assessment of yield variation and its determinants in smallholder African systems," *Proc. Nat. Acad. Sci.*, vol. 114, no. 9, pp. 2189–2194, Feb. 2017.

[7] A. D. Baez-Gonzalez *et al.*, "Large-area maize yield forecasting using leaf area index based yield model," *Agronomy J.*, vol. 97, no. 2, pp. 418–425, Mar. 2005.

[8] X. Zhang and Q. Zhang, "Monitoring interannual variation in global crop yield using long-term AVHRR and MODIS observations," *ISPRS J. Photogrammetry Remote Sens.*, vol. 114, pp. 191–205, Apr. 2016.

[9] L. S. Unganai and F. N. Kogan, "Drought monitoring and corn yield estimation in Southern Africa from AVHRR data," *Remote Sens. Environ.*, vol. 63, no. 3, pp. 219–232, Mar. 1998.

[10] J. M. Deines, R. Patel, S.-Z. Liang, W. Dado, and D. B. Lobell, "A million kernels of truth: Insights into scalable satellite maize yield mapping and yield gap analysis from an extensive ground dataset in the US corn belt," *Remote Sens. Environ.*, vol. 253, Feb. 2021, Art. no. 112174.

[11] F. Gao, M. C. Anderson, and D. Xie, "Spatial and temporal information fusion for crop condition monitoring," in *Proc. IEEE Int. Geosci. Remote Sens. Symp.*, 2016, pp. 3579–3582.

[12] J. Meng, X. Du, and B. Wu, "Generation of high spatial and temporal resolution NDVI and its application in crop biomass estimation," *Int. J. Digit. Earth*, vol. 6, no. 3, pp. 203–218, May 2013.

[13] J. Walker, K. de R. Beurs, R. Wynne, and F. Gao, "Evaluation of landsat and MODIS data fusion products for analysis of dryland forest phenology," *Remote Sens. Environ.*, vol. 117, pp. 381–393, Feb. 2012.

[14] J. Li and D. Roy, "A global analysis of Sentinel-2 A, Sentinel-2B and Landsat-8 data revisit intervals and implications for terrestrial monitoring," *Remote Sens.*, vol. 9, no. 9, Aug. 2017, Art. no. 902.

[15] M. Claverie *et al.*, "The harmonized landsat and Sentinel-2 surface reflectance data set," *Remote Sens. Environ.*, vol. 219, pp. 145–161, Dec. 2018.

[16] G. Dedieu *et al.*, "VENμS: Performances and first results after 11 months in orBIT," in *Proc. IEEE Int. Geosci. Remote Sens. Symp.*, 2018, pp. 7756–7759.

[17] M. Gašparović , D. Medak, I. Pilaš , L. Jurjević, and I. Balenović, "Fusion of Sentinel-2 and planetscope imagery for vegetation detection and monitoring" *Int. Arch. Photogrammetry Remote Sens. Spatial Inf. Sci.*, vol. XLII- 1, pp. 155–160, Sep. 2018.

[18] R. Gurdak and P. Grzybowski, "Feasibility study of vegetation indices derived from Sentinel-2 and PlanetScope satellite images for validating the LAI biophysical parameter to monitoring development stages of winter wheat," *Geoinformat. Issues*, vol. 10, no. 1, pp. 27–35, 2018.

[19] D. Ichikawa and K. Wakamori, "The integrated use of landsat, Sentinel-2 and PlanetScope satellite data for crop monitoring," in *Proc. IEEE Int. Geosci. Remote Sens. Symp.*, 20182018, 7707–7710.

[20] Y. Sadeh, X. Zhu, K. Chenu, and D. Dunkerley, "Sowing date detection at the field scale using CubeSats remote sensing," *Comput. Electron. Agriculture*, vol. 157, pp. 568–580, Feb. 2019.

[21] A. Kross, H. McNairn, D.Lapen, M. Sunohara, and C. Champagne, "Assessment of RapidEye vegetation indices for estimation of leaf area index and biomass in corn and soybean crops," *Int. J. Appl. Earth Observ. Geoinformation*, vol. 34, pp. 235–248, Feb. 2015.

[22] H. A. Ali, D. Delparte, and L. M. Griffel, "From pixel to yield: Forecasting potato productivity in Lebanon and Idaho" *Int. Arch. Photogrammetry Remote Sens. Spatial Inf. Sci.*, vol. XLII-3/W11, pp. 1–7, Feb. 2020.

[23] M. C. F. Wei, L. F. Maldaner, P. M. N. Ottoni, and J. P. Molin, "Carrot yield mapping: A precision agriculture approach based on machine learning," *AI*, vol. 1, no. 2, pp. 229–241, Jun. 2020.

[24] S. Skakun *et al.*, "Assessing within-field corn and soybean yield variability from WorldView-3, planet, Sentinel-2, and Landsat 8 satellite imagery," *Remote Sens.*, vol. 13, no. 5, p. 872, Feb. 2021.

[25] R. Houborg and M. F. McCabe, "A cubesat enabled spatio-temporal enhancement method (CESTEM) utilizing planet, landsat and MODIS data," *Remote Sens. Environ.*, vol. 209, pp. 211–226, May 2018.

[26] F. Gao *et al.*, "A within-season approach for detecting early growth stages in corn and soybean using high temporal and spatial resolution imagery," *Remote Sens. Environ.*, vol. 242, Jun. 2020, Art. no. 111752.

[27] A. L. Nguy-Robertson and A. A. Gitelson, "Algorithms for estimating green leaf area index in C3 and C4 crops for MODIS, Landsat TM/ETM, MERIS, Sentinel MSI/OLCI, and Venμs sensors," *Remote Sens. Lett.*, vol. 6, no. 5, pp. 360–369, May 2015.

[28] T. Kharel *et al.*, "Yield monitor data cleaning is essential for accurate corn grain and silage yield determination," *Agronomy J.*, vol. 111, no. 2, pp. 509–516, Mar. 2019.

[29] K. A. Sudduth, S. T. Drummond, and D. B. Myers, "Yield editor 2.0: Software for automated temoval of yield map errors," *ASABE Annual Int. Meet.*, Dallas, Texas, Jul.-Aug. 2012.

[30] F. Gao *et al.*, "Toward mapping crop progress at field scales through fusion of landsat and MODIS imagery," *Remote Sens. Environ.*, vol. 188, pp. 9–25, Jan. 2017.

[31] L. Zhong, L. Hu, L. Yu, P. Gong, and G. S. Biging, "Automated mapping of soybean and corn using phenology," *ISPRS J. Photogrammetry Remote Sens.*, vol. 119, pp. 151–164, Sep. 2016.

[32] E. Myers, J. Kerekes, C. Daughtry, and A. Russ, "Assessing the impact of satellite revisit rate on estimation of corn phenological transition timing through shape model fitting," *Remote Sens.*, vol. 11, no. 21, Oct. 2019, Art. no. 2558.

[33] J. Chen, P. Jönsson, M. Tamura, Z. Gu, B. Matsushita, and L. Eklundh, "A simple method for reconstructing a high-quality NDVI time-series data set based on the Savitzky-Golay filter," *Remote Sens. Environ.*, vol. 91, no. 3/4, pp. 332–344, Jun. 2004.

[34] S. Mourtzinis, F. J. Arriaga, K. S. Balkcom, and B. V. Ortiz, "Corn grain and stover yield prediction at R1 growth stage," *Agronomy J.*, vol. 105, no. 4, pp. 1045–1050, 2013.

[35] S. L. Osborne, J. S. Schepers, and M. R. Schlemmer, "Using multi-spectral imagery to evaluate corn grown under nitrogen and drought stressed conditions," *J. Plant Nutrition*, vol. 27, no. 11, pp. 1917–1929, 2004.

[36] J. F. Shanahan *et al.*, "Use of remote-sensing imagery to estimate corn grain yield," *Agronomy J.*, vol. 93, no. 3, pp. 583–589, 2001.

[37] A. Huete, K. Didan, T. Miura, E. Rodriguez, X. Gao, and L. Ferreira, "Overview of the radiometric and biophysical performance of the MODIS vegetation indices," *Remote Sens. Environ.*, vol. 83, no. 1/2, pp. 195–213, Nov. 2002.

[38] Z. Jiang, A. Huete, K. Didan, and T. Miura, "Development of a two-band enhanced vegetation index without a blue band," *Remote Sens. Environ.*, vol. 112, no. 10, pp. 3833–3845, Oct. 2008.

[39] A. Gitelson, Y. Gritz, and M. N. Merzlyak, "Relationships between leaf chlorophyll content and spectral reflectance and algorithms for non-destructive chlorophyll assessment in higher plant leaves," *J. Plant Physiol.*, vol. 160, no. 3, pp. 271–282, Jan. 2003.

[40] J. Rouse, R. Haas, J. Schell, and D. Deering, "Monitoring vegetation systems in the great plains with ERTS," NASA, Greenbelt, MD, USA, Rep. no. PAPER-A20, 1973.

[41] A. Huete, "A soil-adjusted vegetation index (SAVI)," *Remote Sens. Environ.*, vol. 25, no. 3, pp. 295–309, Aug. 1988.
[42] A. A. Gitelson, "Wide dynamic range vegetation index for remote quantification of biophysical characteristics of vegetation," *J. Plant Physiol.*, vol. 161, no. 2, pp. 165–173, Jan. 2004.
[43] F. Gao, M. Anderson, C. Daughtry, and D. Johnson, "Assessing the variability of corn and soybean yields in central Iowa using high spatiotemporal resolution multi-satellite imagery," *Remote Sens.*, vol. 10, no. 9, Sep. 2018, Art. no. 1489.
[44] S. N. Goward, T. V. Loboda, D. L. Williams, and C. Huang, "Landsat orbital repeat frequency and cloud contamination: A case study for eastern United States," *Photogrammetric Eng. Remote Sens.*, vol. 85, no. 2, pp. 109–118, Feb. 2019.
[45] D. P. Roy, H. Huang, R. Houborg, and V. S. Martins, "A global analysis of the temporal availability of PlanetScope high spatial resolution multi-spectral imagery," *Remote Sens. Environ.*, vol. 264, Oct. 2021, Art. no. 112586.

Emily Myers (Member, IEEE) received the B.A. degree in physics from New College of Florida, Sarasota, FL, USA, in 2013. She is currently working toward the Ph.D. degree in imaging science with the Rochester Institute of Technology, Rochester, NY, USA.

She was an Intern with Oak Ridge National Laboratory, Oak Ridge, TN, USA, in 2019, where she was involved in research into shadow and water detection in multispectral imagery. Her research interests include ecological remote sensing and image time-series analysis.

Ms. Myers is a Member of Out in Science, Technology, Engineering, and Mathematics.

John Kerekes (Senior Member, IEEE) received the B.S., M.S., and Ph.D. degrees in electrical engineering from Purdue University, West Lafayette, IN, USA in 1983, 1986, and 1989.

From 1983 to 1984, he was a member of the Technical Staff with the Space and Communications Group, Hughes Aircraft Co., El Segundo, CA, USA, where he performed circuit design for communications satellites. From 1986 to 1989, he was a Graduate Research Assistant, working with both the School of Electrical Engineering and the Laboratory for Applications of Remote Sensing, Purdue University. From 1989 to 2004, he was a Technical Staff Member with the Lincoln Laboratory, Massachusetts Institute of Technology, Lexington, MA, USA. Since 2004, he has been with the Chester F. Carlson Center for Imaging Science, Rochester Institute of Technology, Rochester, NY, USA, where he is currently a Research Professor. His research interests include the modeling and analysis of remote sensing system performance in pattern recognition and geophysical parameter retrieval applications.

Dr. Kerekes is a Member of Tau Beta Pi, Eta Kappa Nu, the American Geophysical Union, and the American Society for Photogrammetry and Remote Sensing. He is a Senior Member of SPIE. He was the recipient of the GRSS Outstanding Service Award, in 2017. From 2010 to 2015 he served on the GRSS Administrative Committee (AdCom). He is currently serving as the GRSS Chief Financial Officer. From 1995 to 2004, he served as the founding Chair of the Boston Section Chapter of the IEEE Geoscience and Remote Sensing Society (GRSS), and from 2007 to 2010 he served as the founding Chair of the Western New York Chapter of GRSS. He was a Co-General Chair of IGARSS 2008 held in Boston, MA, USA.

Craig Daughtry received the B.S. and M.S. degrees in agronomy from University of Georgia, Athens, GA, USA, in 1972 and 1974, respectively, and the Ph.D. degree in agronomy (crop physiology) from Purdue University, West Lafayette, IN, USA, in 1976.

From 1976 to 1987, he was a Research Agronomist working with both the Agronomy Department and the Laboratory for Applications of Remote Sensing at Purdue University. From 1987 to 2021, he was a Research Agronomist with the Hydrology and Remote Sensing Laboratory of the Agricultural Research Service of the United States Department of Agriculture, in Beltsville, MD, USA. His research interests include measuring and modeling the spectral and biophysical properties of crops and soils.

Dr. Daughtry is a Fellow of the American Society of Agronomy.

Andrew L. Russ was born in Alexandria, VA, USA, in 1965. He received the B.S. degree in biology from the University of Maryland, College Park, MD, USA, in 1993, and the M.A. degree in geography from the University of Maryland, College Park, MD, USA in 2003.

From 1994 to present, he has been with the United States Department of Agriculture's Beltsville Agricultural Research Center, Beltsville, MD, USA.

Mr. Russ is a Member of the American Society of Agronomy.